Acquisition of object and temperature series in medium resolution off-axis electron holography with live drift correction

Thibaud Denneulin[a,], Benjamin Zingsem[a], Joseph Vas[a], Wen Shi[a], Luyan Yang[a], Michael Feuerbacher[a], Rafal E. Dunin-Borkowski[a]

[a]*Ernst Ruska-Centre for Microscopy and Spectroscopy with Electrons, Forschungszentrum Jülich, 52425 Jülich, Germany.*

Abstract

Collecting and averaging large datasets is a common practice in transmission electron microscopy to improve the signal-to-noise ratio. Averaging data in off-axis electron holography requires automated tools capable of correcting both the drift of the interference fringes and the drift of the specimen. This can be achieved either off-line, by post-processing hologram series, or on-line, through real-time microscope control. For on-line correction, a previously suggested method involves independently adjusting the position of the intereference fringes and the sample by controlling the beam tilt coils and the stage during hologram acquisition. In this study, we have implemented this on-line correction method in a Thermo Fisher Scientific Titan transmission electron microscope. The microscope is equipped with a piezo-enhanced CompuStage for positioning the sample with high precision. However, the control of the piezo stage via direct scripting is not supported. We first describe a workaround to enable automated sample position correction. We then demonstrate the benefits of live, program-controlled acquisitions for serial experiments in medium resolution off-axis electron holography. Application examples include the automatic acquisition of an object series such as a transistor array and an *in-situ* temperature series of magnetic skyrmions.

Keywords: Electron holography, automation, drift correction, piezo stage.
PACS: 68.37.Lp, 61.05.jp
2008 MSC: ...

---

1. Introduction

Off-axis electron holography is a transmission electron microscopy (TEM) technique that uses an electron biprism to overlap a wave passing through a sample with a reference wave traveling in vacuum [1, 2]. The hologram recorded on a camera is then processed using Fourier transforms to reconstruct the phase of the electron wave, which is not available in a conventional TEM image (basic equations are recalled in Supplementary Information 1). Electron holography can be used to explore different topics such as high resolution imaging [3, 4], electrostatic fields in doped semiconductors [5, 6], domains in magnetic materials [7, 8] or strain in epitaxial samples [9, 10]. In order to improve the signal-to-noise ratio in the phase images, it is common to increase the exposure time to as long as the stability of the microscope and the sample allows. The smallest measurable phase difference $\delta\phi$ and the square root of the mean number of electrons per pixel $\sqrt{N}$ follow an inverse relationship $\delta\phi \propto 1/(C\sqrt{N})$ where C is the fringe contrast [11]. In practice, the maximum exposure time can vary significantly between a few seconds and a few minutes depending on the drift of the specimen and the holographic fringes [12, 13, 14].

Email address: `t.denneulin@fz-juelich.de` (Thibaud Denneulin)

One method to circumvent this limit is to acquire multiple holograms and to align them using post-processing reconstruction methods, which has been discussed in several articles [14, 15, 16, 17]. Another method developed by Gatel et al. [18] in a Hitachi microscope consists in using live correction mechanisms to continuously realign the microscope during the acquisition, which has the advantage of reducing the amount of data collected. In this method, the position of the fringes and the sample on a camera is controlled independently using the beam tilt coils and the stage. Here, we first describe how this method can be set up in a Thermo Fisher Scientific (TFS) Titan microscope equipped with a piezo-enhanced CompuStage. This stage combines mechanical and piezo motors for positioning the sample with high precision. However, script commands for controlling the piezo stage are missing. Therefore, we have first written a program that can automatically input coordinates in the user interface of the piezo stage. This program was combined with Digital Micrograph scripts to monitor and correct the position of the sample and the fringes on a Gatan camera. We then describe the advantages of this method for serial acquisitions in particular for object and temperature series in medium resolution holography. The first application example is the automatic acquisition of a transistor array, which involves a combination of mechanical and piezo stage movements. The second example is the correction of heating-induced drift during the acquisition of a temperature series of magnetic skyrmions using an *in-situ* heating holder.

2. Methods

2.1. Instrumentation

Experiments were carried out using a TFS Titan TEM equipped with a Schottky field emission gun operated at 300 kV, a piezo-enhanced CompuStage, a CEOS image aberration corrector, a post-specimen electron biprism and a 4k×4k Gatan K2-IS direct electron detector [19]. The microscope was operated in Lorentz mode by setting the objective lens to zero and using the first transfer lens of the aberration corrector as the main imaging lens. The condenser stigmators were used to form an elliptical illumination to improve the coherence in the direction perpendicular to the biprism.

Fig. 1(a) shows a picture of the piezo-enhanced compustage (additional images are shown in Supplementary Information 2). It includes three piezo motors coupled to the three mechanical axes. The mechanical axes have a large range of approximately 1 mm in x and y directions. However, we found that the smallest step size is in the 5-10 nm range (see Supplementary Information 3), which is too large for applications in medium resolution. The range of the piezo components is approximately 1.5 µm in x/y with a step size as fine as 20 pm according to the description of TFS. In the TEM user interface, the “Stage Piezo” panel shown in Fig. 1(b) displays the x, y, z coordinates in percentage. It includes a flap-out panel with three different tabs labeled “Control” shown in Fig. 1(c), “Move” in Fig. 1(d) and “Jog” (not used in this study). The “Control” tab allows the activation/deactivation of the piezo stage and the measuring unit. The “Move” tab allows the input of coordinates in the “Setpoint[%]” column. The coordinates can also be changed via the multi-functions and the focus knobs on the control pads.

2.2. Scripting

We did not find script commands to control the piezo stage neither in Digital Micrograph (DM Gatan) scripting nor in TFS TEM Scripting. Therefore, to control the piezo stage in an automated way, we have written a Microsoft Windows program that can fill automatically the x, y, z “Setpoint[%]” coordinates in the user interface. The program was written using AutoHotkey, which is a free scripting language that can be used to emulate mouse clicks and keystrokes. When the program is active, it runs in the background and

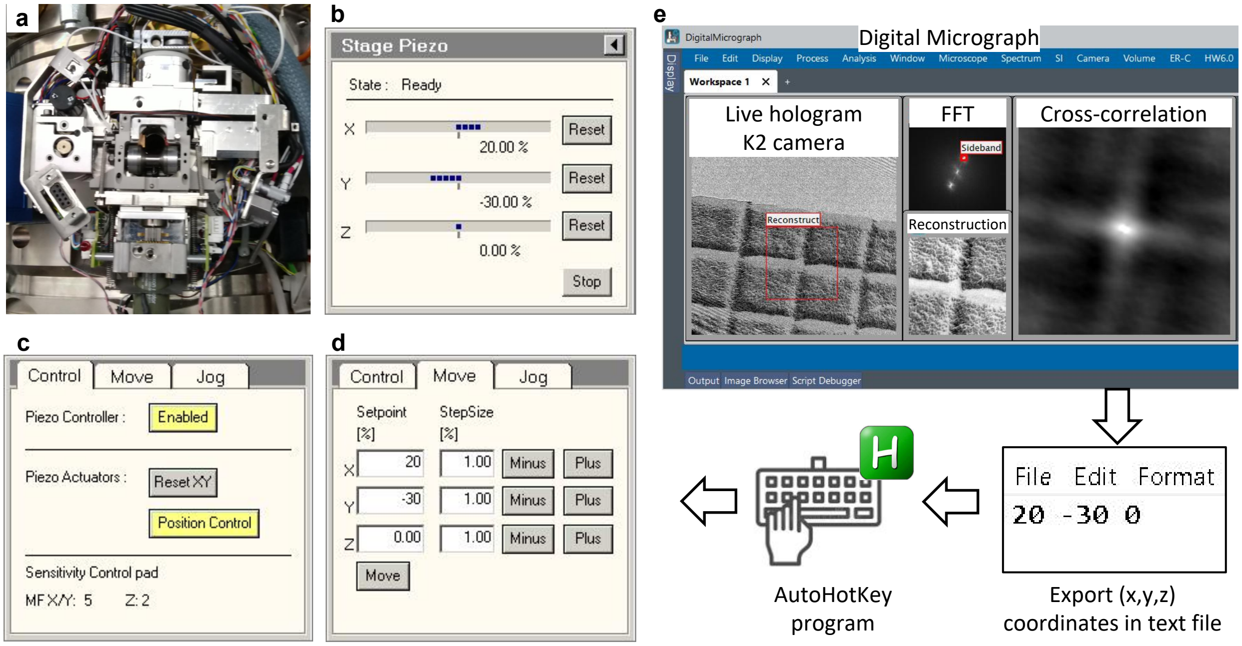

State : Ready
X 20.00 %
Y -30.00 %
Z 0.00 %

Piezo Controller : Enabled
Piezo Actuators :
Sensitivity Control pad
MF X/Y: 5 Z: 2

	Setpoint [%]	StepSize [%]
X	20	1.00
Y	-30	1.00
Z	0.00	1.00

```
20 -30 0
```

Figure 1: **Control sequence of the piezo stage.** (a) Picture of the CompuStage. (b) Screen capture of the "Stage Piezo" panel in the user interface that shows the actual x, y, z coordinates. (c) Screen capture of the sub-panel that allows the activation/deactivation of the piezo stage and the measuring unit. (d) Screen capture of the sub-panel that allows the manual input of the coordinates. (e) Schematic that shows the principle of the sample drift correction. A script in Digital Micrograph captures holograms from the live view of the camera; an amplitude or phase image is reconstructed using Fourier transformations; a cross-correlation is performed to measure any displacement of the specimen; new coordinates are written in a text file; the AutoHotkey program fills automatically the new coordinates in the panel shown in (d).

checks continuously for the presence of a text file in a predefined folder. When a file is detected, the program places the cursor placed successively in the three cells of the "Setpoint[%]" column, emulates key strokes to enter the coordinates and clicks on the "Move" button to activate the piezo motors.

Digital Micrograph was used to capture and process holograms using DM scripting. Functions of the Holoworks plugin [20] were used to perform Fast Fourier transforms (FFT), side-band detections, phase and amplitude reconstructions on-the-fly. The general workflow of the drift correction is the following. Holograms are captured from the live view of the camera. To determine the position of the holographic fringes in the image, a first FFT is calculated in a small region of the hologram to minimize computing time, preferably in a region that shows a high fringe contrast (in vacuum for instance). The pixel in the side-band that shows the largest modulus is located, the associated phase value is calculated and compared with the phase of the first hologram. The correction is then achieved using the beam tilt coils. A preliminary calibration step is carried out to determine the relationship between beam tilt and phase shift before the experiment (see Supplementary Information 4). To monitor the position of the sample, a second FFT is performed in a small region of the sample that shows distinct features. An amplitude or phase image is reconstructed and a cross-correlation is performed to measure the displacement. A text file containing new coordinates is then exported and the coordinates are transferred to the piezo stage via the AutoHotkey program as shown schematically in Fig. 1(e). A preliminary calibration step is carried out to determine the relation between the pixel grid of the camera and the coordinates of the piezo stage (see Supplementary Information 5). The aligned holograms are summed iteratively in real space. The noise in the summed hologram is monitored by reconstructing a phase image in a small uniform region and calculating its standard deviation after phase

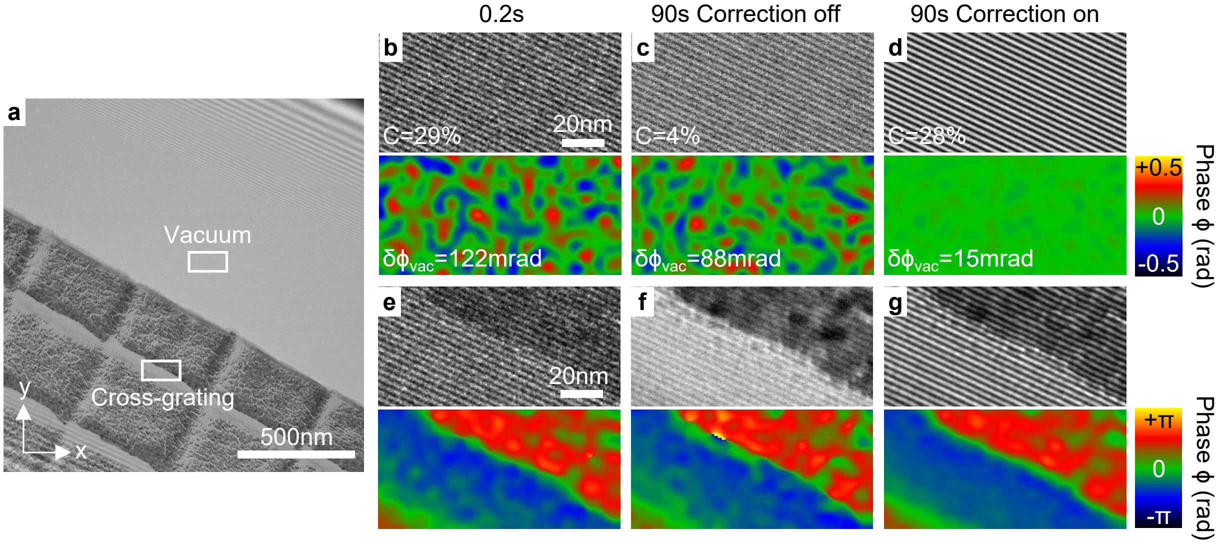

Figure 2: **Drift-corrected acquisition test.** (a) Example of off-axis electron hologram of a cross grating replica sample. (b-d) Magnified images of the hologram in the vacuum region indicated by a rectangle in (a) for different acquisition conditions of 0.2 s, 90 s without correction and 90 s with correction of the fringe position using the beam tilt and correction of the sample position using the piezo stage. Corresponding phase images reconstructed using Fourier transforms with an aperture size of $q_c/3$ are shown at the bottom. (e-g) Magnified images of the hologram in the cross grating region and corresponding phase images for the same conditions.

unwrap and subtraction of linear phase wedges. The different scripting operations are performed sequentially in a single thread.

2.3. *Drift correction example*

Fig. 2(a) shows an example of drift corrected acquisition using a gold coated cross grating replica sample. The holographic fringe spacing is 2.7 nm and the pixel size of 0.41 nm. The sample is visible in the bottom-left part of the image and the top-right part shows a vacuum region. Fig. 2(b-d) shows magnified images of the vacuum region and corresponding phase images for different acquisition conditions of 0.2 s, 90 s without correction, and 90 s with correction of the fringe position and sample position. For 90 s exposures, a total of 450 frames with an individual exposure time of 0.2 s were summed iteratively during the experiment. However, there was an interval of approximately 2 s between two consecutive frames due to times required to process each hologram, set the beam tilt and the piezo corrections. The fringe contrast, defined as $C = (I_{\max} - I_{\min})/(I_{\max} + I_{\min})$ where $I_{\max}$ and $I_{\min}$ are the maximum and minimum of intensity of the fringes, is respectively 29%, 4% and 28% for the three different acquisitions. The contrast obtained with 90 s exposure and without correction is then significantly lower than the contrast obtained with a short exposure due to the drift of the fringes. On the other hand, the contrast with correction is nearly the same as that obtained with a short exposure. Consequently, the noise in the phase image with correction is significantly reduced thanks to both the high contrast and a large number of counts. The standard deviation $\delta\phi_{\mathrm{vac}}$ is respectively 122 mrad for 0.2 s, 88 mrad for 90 s without correction and 15 mrad with correction. Similarly, the comparison of the holograms obtained on the sample (e-g) shows a better quality with correction and the phase image is smoother.

For a more detailed interpretation, Fig. 3 shows different plots that represent in (a) the position of the fringes ϕ, (b) the standard deviation of the phase image in the vacuum $\delta\phi_{vac}$ and (c) the position of the sample (x,y) as a function of exposure time. Without correction, the position of the fringes ϕ drifted by

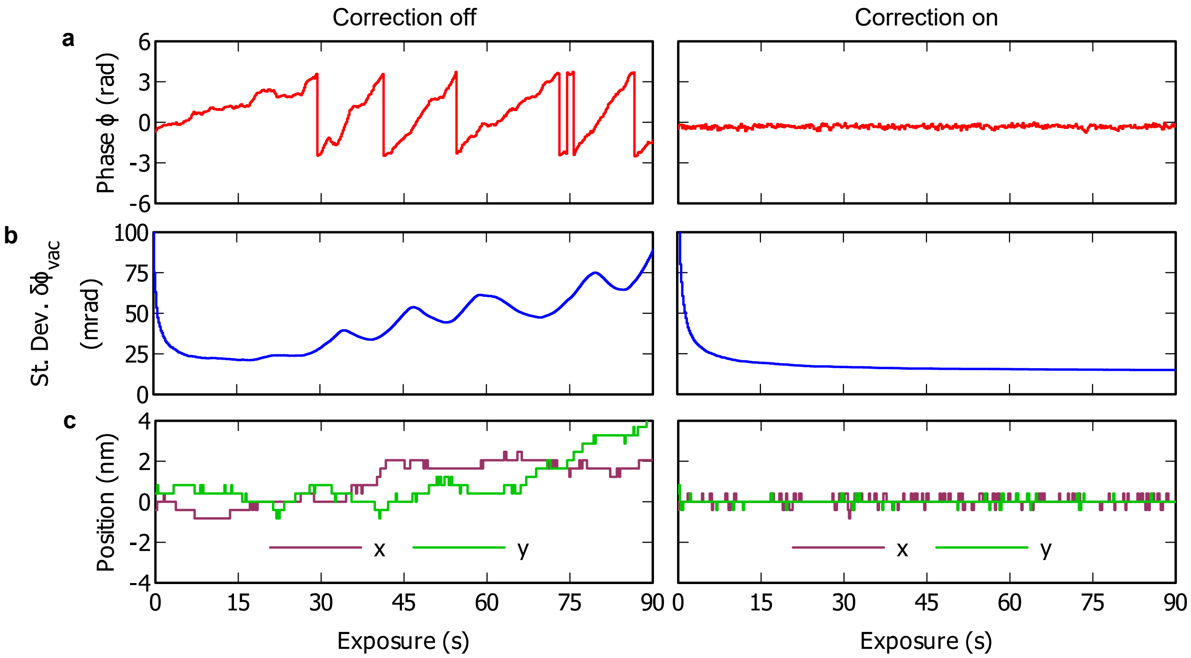

Figure 3: **Drift-corrected acquisition test (monitoring profiles).** (a) Position of the fringes (in rad between $+\pi$ and $-\pi$), (b) standard deviation of the phase in the vacuum $\delta\phi_{\text{vac}}$ and (c) lateral position of the sample (x,y) as a function of exposure time, without (left) and with correction (right).

approximately 28 rad over the entire experiment. Consequently, the standard deviation $\delta\phi_{\text{vac}}$ oscillates as a function of time. It increases when the drift is close to $\pm\pi$ and decreases when it comes back to zero (or 2π). With correction, the position of the fringes remained stable over the entire exposure with a precision of ±0.1 rad (standard deviation of the plot). $\delta\phi_{\text{vac}}$ decreases continuously as a function of exposure time following an inverse relationship and tends towards a limit of approximately 15 mrad. Depending on the position and the size of the area in which $\delta\phi_{\text{vac}}$ is calculated, Fresnel fringes and non-linear distortions [21] can contribute to such time-independent limit because no reference hologram was used during live reconstructions. Nevertheless, this value is comparable to values reported previously with a similar method on a different microscope [22]. The position profiles (x,y) show a notched shape with notches of ±0.41 nm because the position of the sample was determined with pixel precision. The sample was quite stable even without correction, most likely because it was inserted in the microscope a long time before the experiment was carried out. Nevertheless, without correction, small deviations of the position of up to 4 nm in x and 2 nm in y were measured. With correction, the position of the sample was maintained fixed with ±1 pixel (or ±0.41 nm) precision.

In Supplementary Information 6, we were also able to record phase-shifted hologram series (including double-resolution holograms) and maintain the position of the sample during the different shifts to improve the spatial resolution of the reconstructed phase images [23, 24]. In Supplementary Information 7, we tested the same drift correction method in objective mode with 0.4 nm holographic fringes and 0.06 nm pixel size. We were able to correct the position of the fringes and the sample with precisions of ±0.3 rad and ±0.2 nm respectively.

3. Applications

3.1. Object series

Here, the live correction method is applied to the acquisition of an object series. The sample is an array of dummy MOSFET transistors as shown in Fig. 4(a). Each transistor consists of a 30 nm large Si channel with recessed $Si_{0.77}Ge_{0.23}$ source/drain grown by reduced pressure chemical vapor deposition (RP-CVD) [25] and a gate stack of SiO_2/Si_3N_4 (see bottom image in Fig. 4(a)). The cross-section lamella was prepared using a Ga^+ focused ion beam and scanning electron microscope (FIB-SEM) machine. The distance between two transistors is approximately 500 nm and the 5 µm long electron transparent region of the lamella shows 25 transistors. The goal is to collect automatically and sum holograms of the 25 transistors to improve statistically the signal-to-noise ratio in the phase images. For this goal, we have written a script that uses the mechanical stage for the coarse movements *i.e.* to move from one transistor to another, and the piezo stage for fine movements *i.e.* to adjust the position of the sample within the field of view using the first hologram as a reference. The coarse movement is performed in a single step whereas the fine movement of the piezo stage is continuously monitored and adjusted during the experiment, as described in the previous section. The correction was based on cross-correlations of phase images instead of amplitude images because it gave more reliable results for this sample (see Supplementary Information 8). The following parameters were used, fringe spacing 2.7 nm, pixel size 0.41 nm, individual exposure time 0.4 s and 40 frames per transistor (total 20 s exposure). However, as it can take a few iterations for the piezo stage to converge after a large mechanical movement (see Supplementary Information 3), 10 additional frames per transistor with active correction were added to the script but the frames were not included in the summed hologram. During the entire experiment, the position of the fringes in the Si substrate was monitored and corrected continuously using the beam tilt. In total, the experiment lasted approximately 45 mins.

Fig. 4(b) shows an example of electron hologram of a single transistor and Fig. 4(c) shows the average hologram of 25 transistors. The fringe contrast is the same in both cases ($C = 36\%$), which indicates that the position of the fringes remained stable during the different acquisitions. Fig. 4(d,e) shows the corresponding phase images of the two holograms, where the phase shifts observed in the source/drain and the gate regions with respect to the substrate are essentially related to the different mean inner potential of the materials. The standard deviation of the phase measured in the substrate $\delta\phi_{\mathrm{Si}}$ (dashed rectangle) is 35 mrad for the hologram of a single transistor and 18 mrad for the average hologram. The decrease of the standard deviation as a function of the number of averaged transistors is reported on the plot in Fig. 4(f). The limit of 18 mrad indicated by a dashed line is reached by averaging over 15 transistors. This limit indicates the presence of time- and sample-independent phase variations, as measured also in the vacuum in Fig. 3(b). Besides the improvement of the signal-to-noise ratio, additional statistical information can be obtained about the transistors such as dispersion. Fig. 4(g) shows the standard deviation of the 25 phase images. It shows a relatively large value at the sides of the gate, which indicates that the width of the gate varies from one transistor to the other.

To describe this experiment in more detail, Fig. 5 shows four plots that represent in (a) the position of the fringes ϕ, (b) the standard deviation of the phase measured in the substrate $\delta\phi_{\mathrm{Si}}$, (c) the distance traveled by the mechanical stage and (d) the position (x,y) of the transistor in the image with respect to the position of the first transistor as a function of exposure time. It can be observed that the position of the fringes ϕ remained stable with a precision of ±0.3 rad and only one exceptional perturbation occurred at 180 s. This value of standard deviation is slightly higher than in the previous experiment, which is related to the fact that the position of the fringes was monitored in the Si substrate instead of the vacuum because of the presence

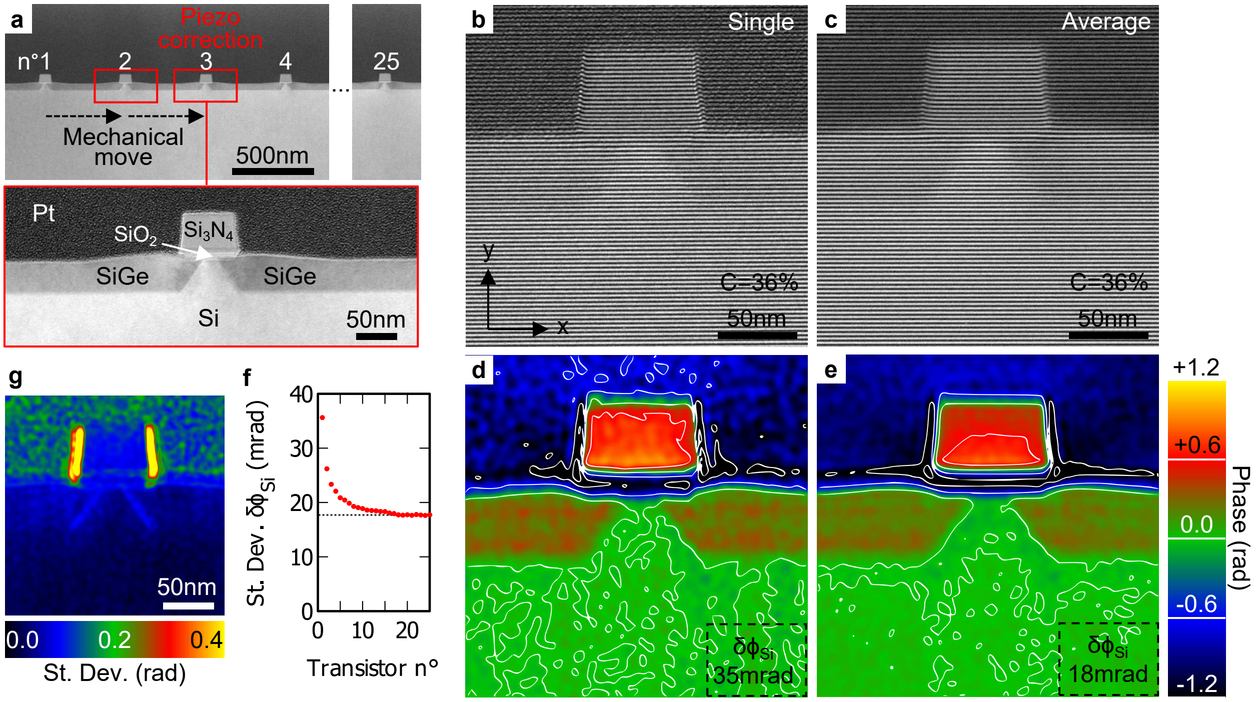

Figure 4: **Automated acquisition of a transistor series.** (a) Low-mag TEM image of a series of dummy MOSFET transistors with recessed $Si_{0.77}Ge_{0.23}$ source/drain and a gate of SiO_2/Si_3N_4. The image at the bottom shows a magnified view of a single transistor. (b) Example of electron hologram recorded for 16 s on a single transistor. (c) Average electron hologram of 25 different transistors. (d,e) Phase images reconstructed from the holograms (b,c) respectively. (f) Standard deviation of the phase measured in the substrate $\delta\phi_{Si}$ as a function of the number of averaged transistors. (g) Standard deviation of the 25 phase images.

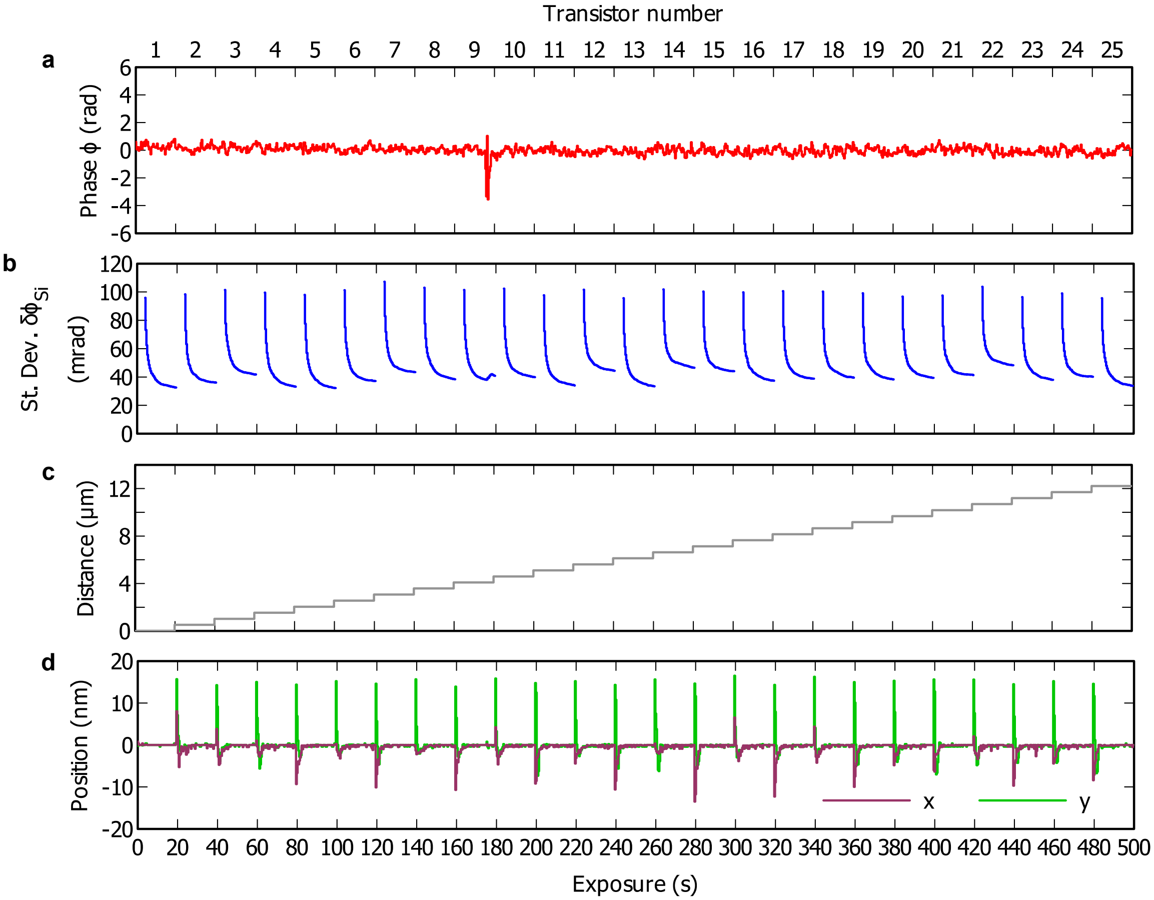

Figure 5: **Automated acquisition of a transistor series (monitoring profiles).** (a) Position of the fringes ϕ, (b) standard deviation of the phase in the silicon substrate $\delta\phi_{\mathrm{Si}}$, (c) distance traveled by the mechanical stage, (d) position of the transistor (x,y) in the image with respect to the position of the first transistor, as a function of exposure time and transistor number.

of a thick Pt capping layer. The substrate can exhibit local thickness variations due to curtaining effects introduced by FIB preparation [26] in particular below the gate, which can cause small phase variations. For each individual acquisition, the standard deviation $\delta\phi_{\mathrm{Si}}$ decreases following an inverse relationship from 100 mrad down to 30-50 mrad after 16 s of exposure. This last value depends on the transistor mainly because of the local thickness variations in the substrate already mentioned. By summing holograms of different transistors, the effects of curtaining can be statistically minimized and the standard deviation can be further reduced, as shown in Fig. 4(f). The total distance traveled by the mechanical stage over the whole experiment is approximately 12 µm with regular steps of 500 nm. The position of the transistor in the image shows a large offset of up to ±20 nm in x and y after each mechanical movement. Most of the times, this offset is reduced below 1 nm after approximately five piezo correction steps ($\approx$ 2 s exposure time). On close inspection, it can be seen that there is sometimes a slight overcorrection in the first steps after the mechanical move. This might be related to a drift of the sample induced by the mechanical move or an offset in the calibration.

3.2. Temperature series

The piezo stage correction can also be useful for *in-situ* experiments that involve recording holograms as a function of an external stimulus. In this example, the sample is a ferromagnetic alloy of $Co_8Zn_{10}Mn_2$ (CZM) grown using a flux method [27] that hosts skyrmions at room temperature. The presence of skyrmions is related to the non-centrosymmetric crystal structure and the associated Dzyaloshinskii–Moriya interaction [28]. A Gatan double tilt heating holder model 652 and a temperature controller model 1905 connected to the PC of the camera were used to vary the temperature. As the range of the piezo stage is quite short, the amplitude and the direction of the drift when changing the temperature were pre-tested. To optimize the range, the piezo stage was set to 75% in the opposite direction of the drift before the experiment. In order to generate a magnetic skyrmion lattice, the sample was oriented close to a [001] zone-axis and a field cooling procedure was carried out by warming the sample up to the 80°C and cooling it down to room temperature in the presence of a perpendicular magnetic field of 80 mT using the objective lens of the microscope.

The following parameters were used to acquire the temperature series, fringe spacing 2.7 nm, pixel size 0.41 nm, individual exposure time 0.4 s, temperature range of 20°C to 75°C with 5°C steps, 80 frames after each temperature change for drift correction only and 50 frames for both drift correction and acquisition of the hologram (20 s exposure). The experiment took approximately 55 mins to complete. Fig. 6(a) shows an example of electron hologram obtained at 20°C on a lamella of the CZM sample. The Pt capping deposited by FIB was included in the field-of-view of the hologram (in the bottom part of the image) because it contains grainy features that were used to set up the cross-correlation for the drift correction. Fig. 6(b) is the corresponding phase image, which shows a skyrmion lattice in the top part of the image. The area of the sample just below the Pt capping shows damages induced by mechanical polishing of the surface. Fig. 6(c) shows magnified phase images of the region indicated by a dashed square in (b) that contains a group of skyrmions and for different temperatures between 20°C and 70°C. It can be observed that the position of the skyrmions in the image remains the same at different temperatures, indicating that the sample drift correction worked. It should be mentioned that no post-acquisition alignment of the images was done and that only linear phase wedges across the images have been removed. Assuming that the composition of the sample is uniform and that the thickness does not change significantly in this small area ($\approx$ 400 nm large), we can consider that phase changes are related essentially to the magnetic induction field. The phase contrast of the skyrmions decreases continuously when increasing the temperature, which is also visible in the phase profiles in Fig. 6(d) extracted across three skyrmions, due to the weakening of the magnetic field. The skyrmion phase contrast vanishes completely at 70°C, which can indicate that the Curie temperature is reached. It can be noted that there are horizontal streaks in the phase images and they are more visible at 70°C because the contrast is uniform. These are artifacts coming from the camera, possibly indicating that a new gain reference should have been taken. Fig. 6(e) shows color-coded maps indicating the direction of the magnetic induction field that were calculated from the phase gradient. The magnetic field rotates around the core of the skyrmions indicating a Bloch-type texture.

Fig. 7 shows four plots that describe the experiment with in (a) the temperature, (b) the position of the fringes ϕ, (c) the standard deviation of the phase in the vacuum $\delta\phi_{\mathrm{vac}}$ and (d) the position of the sample (x,y) as a function of exposure time. As mentioned before, the temperature was increased with steps of 5°C from 20°C to 75°C and it takes approximately 20 frames (8 s exposure time) for the temperature to stabilize. The position of the fringes ϕ was maintained constant for each temperature step with a precision of ± 0.2 rad thanks to the beam tilt correction. However, jumps of more than 2π were observed when changing the temperature (see peaks in the profile) and they could not be corrected. One minor consequence is that the position of the Fresnel fringes at the edge of the hologram was not exactly the same at different temperatures. The standard deviation of the phase measured in the vacuum $\delta\phi_{\mathrm{vac}}$ decreased continuously for each exposure, which confirms that the fringe correction worked well. However, an increase of the standard deviation was

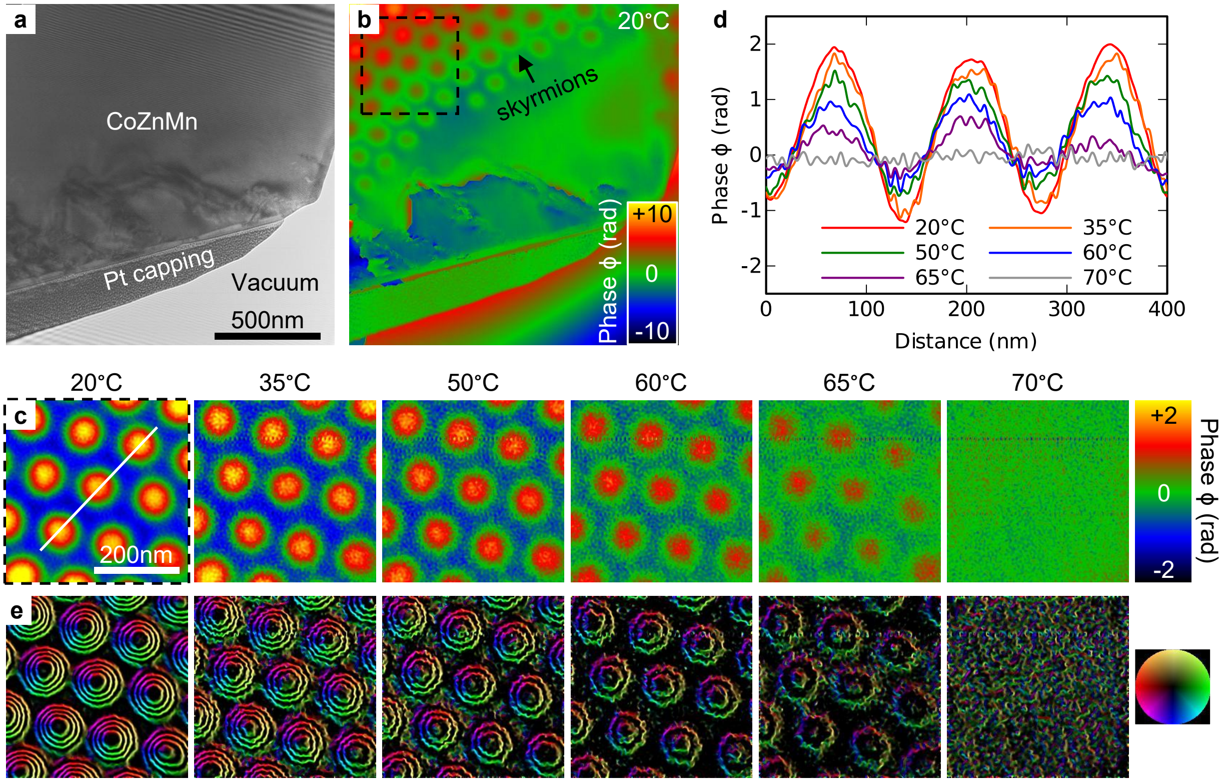

Figure 6: **Automated acquisition of a temperature series of magnetic skyrmions.** (a) Example of electron hologram recorded for 20 s on a sample of $Co_8Zn_{10}Mn_2$ at 20°C in the presence of an external magnetic field of 80 mT. (b) Reconstructed phase image. (c) Magnified phase images of a group of skyrmions in the region indicated by a dashed square in (b) as a function of the temperature and after removal of linear phase wedges. (d) Phase profiles extracted from the images in (c) along the white line. (e) Color-coded magnetic induction maps with a contour spacing of $2\pi/9$.

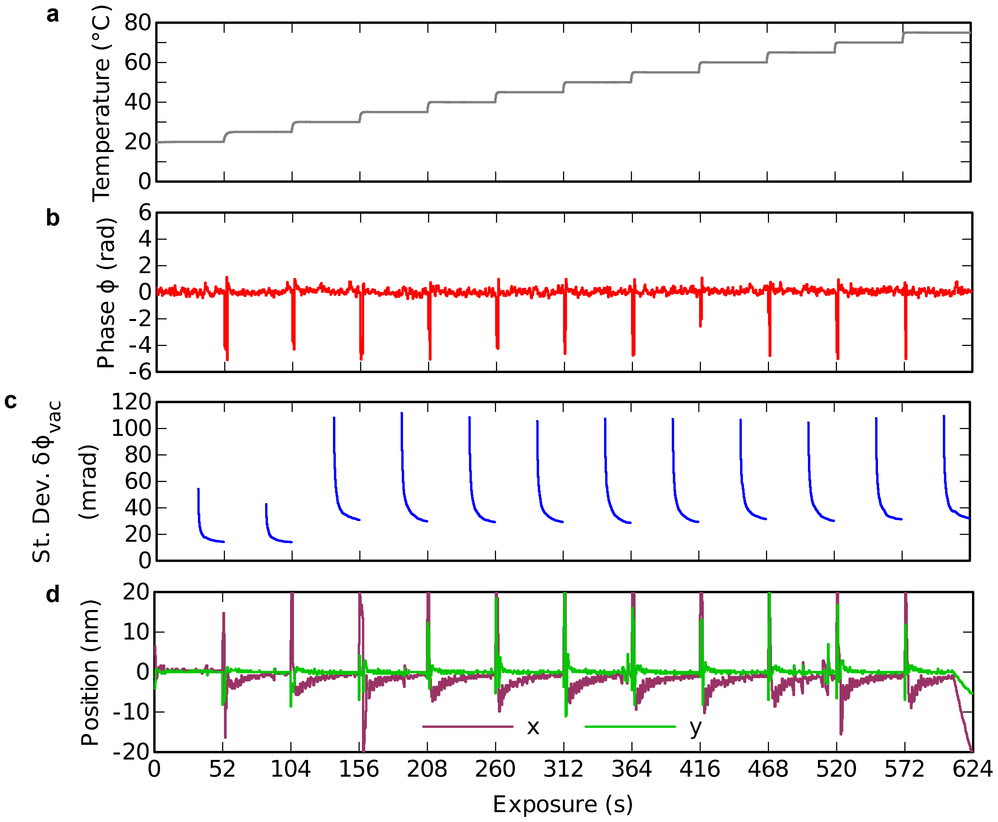

Figure 7: **Automated acquisition of a temperature series of magnetic skyrmions (monitoring profiles).** (a) Temperature, (b) position of the fringes ϕ, (c) standard deviation of the phase in the vacuum $\delta\phi_{\mathrm{vac}}$ and (d) position of the sample (x,y) as a function of exposure time.

observed at 30°C and above compared to room temperature. This phenomenon is related to a decrease of the holographic fringe contrast, which dropped suddenly from $C = 32\%$ to 13% at this temperature. We think that it is a charging phenomenon related to the sample holder because the same observation was made with different samples. After each temperature change, the position of the sample (x,y) shows large disturbances and subsequently a drift appears in the -x direction (up to -10 nm). For this reason, the acquisition of the holograms was delayed after the temperature change so that the position of the sample becomes more stable. The piezo stage brings it back progressively in the $+x$ direction as the drift reduces over time. After the delay of 80 frames (32 s exposure time), the displacement is usually reduced to 1-2 nm. Finally, during the last heating step of 75°C, at approximately 600 s exposure time, the position of the sample could not be maintained and it drifted away because the range of the piezo stage was exceeded.

4. Discussion

We have implemented a live correction method for off-axis electron holography in a TFS microscope based on the scripted control of a piezo-enhanced compustage and the beam tilt coils. In general, the advantage of the live correction approach over the acquisition of hologram series is the minimization of the data and the post-processing steps. One disadvantage is that it requires a number of operations, including software (Fourier transforms of images) and hardware operations (beam tilt and piezo movement), which can take some time to complete and need to be organized in a well-timed order so that it can converge smoothly.

Here, a couple of frames were skipped during processing times, which could be a problem for beam sensitive samples where the electron dose matters. This can be optimized by choosing carefully the individual exposure time and the number of operations depending on the severity of the drift. In addition, the operations were run sequentially in a single thread and using parallel threads could optimize further the scripts. We were able to correct the drift of the sample and the fringes with precisions as good as ±0.2 nm and ±0.1 rad. The precision of ±0.2 nm is similar to the value reported in [18] using a Hitachi microscope equipped with a mechanical stage only. In our case, however, the smallest step obtained with the mechanical stage was in the 5-10 nm range, which was the main reason to focus on the control of the piezo stage.

This method was then applied to the acquisition of holograms of multiple objects thanks to a combination of mechanical and piezo movements. This can help to perform statistical analysis and improve further the signal-to-noise ratio. Different types of scanning and acquisition scenarios can be scripted depending on the geometry of the samples. It was shown that this approach is particularly relevant for transistors and hence should be of interest for the semiconductor industry where holography is used routinely to map dopants or strain [29]. The limit of this approach is simply the number of observable transistors, which is determined by the width of the electron transparent lamella. It was also shown that this method can be used to correct drifts induced by variations of temperature during *in-situ* heating experiments. This avoids repeated human interactions when acquiring temperature series. It allowed us to observe skyrmions in $Co_8Zn_{10}Mn_2$ from room temperature up to the Curie temperature of 70°C. However, the small range of the piezo stage becomes a problem for large variations of temperatures ($\gtrsim$ 100°C), in particular for bulk heating holders that can suffer from severe drifts. A smart combination of mechanical and piezo stage movements can be a solution to this limited range. On the other hand, for chip based heating holders, the drift is usually small and the piezo stage alone should be sufficient even for large temperature ranges.

5. Conclusion

We have implemented an online correction method for off-axis electron holography in a TFS Titan TEM. The scripted control of the piezo-enhanced compustage and the beam tilt coils allowed us to independently correct the drift of the sample and the fringes. It was shown that this method can be used to automatically collect holograms of multiple objects thanks to a combination of mechanical and piezo stage movements, which facilitates the statistical analysis of the phase images. It was also shown that temperature series can be recorded while correcting automatically for the heating induced drift of the sample.

CRediT authorship contribution statement

Thibaud Denneulin: Conceptualization, Investigation, Methodology, Software, Writing – original draft. **Benjamin Zingsem:** Software, Writing – review and editing. **Joseph Vas:** Methodology, Writing – review and editing. **Wen Shi:** Methodology. **Luyan Yang:** Methodology. **Michael Feuerbacher:** Methodology. **Rafal E. Dunin-Borkowski:** Funding acquisition, Resources.

Declaration of competing interest

The authors declare that they have no known competing financial interests or personal relationships that could have appeared to influence the work reported in this paper.

Acknowledgments

This work was supported by the DARPA TEE program (grant MIPR# HR0011831554); the European Union's Horizon 2020 Research and Innovation Programme (grant 856538, project 3D MAGIC) and (grant 823717, project ESTEEM3); the Deutsche Forschungsgemeinschaft (project ID 405553726 - TRR 270). Robert Nijland, Richard Sugijanto and Michael Pyzik (Thermo Fisher Scientific) are acknowledged for maintaining the microscope and providing relevant information. Jean-Michel Hartmann and David Cooper (CEA-LETI) are acknowledged for providing the transistors. C. Gatel (CEMES-CNRS) is acknowledged for discussion.

Data availability

Data will be made available on request.

References

[1] M. R. McCartney, D. J. Smith, Electron holography: Phase imaging with nanometer resolution, Annual Review of Materials Research 37 (1) (2007) 729–767. doi:10.1146/annurev.matsci.37.052506.084219.
URL `https://doi.org/10.1146/annurev.matsci.37.052506.084219`

[2] H. Lichte, M. Lehmann, Electron holography - basics and applications, Reports on Progress in Physics 71 (1) (2008) 016102. doi:10.1088/0034-4885/71/1/016102.
URL `https://doi.org/10.1088/0034-4885/71/1/016102`

[3] H. Lichte, Electron image plane off-axis holography of atomic structures, Vol. 12 of Advances in Optical and Electron Microscopy, Elsevier, 1991, pp. 25–91. doi:10.1016/B978-0-12-029912-6.50006-3.
URL `https://doi.org/10.1016/B978-0-12-029912-6.50006-3`

[4] M. Linck, B. Freitag, S. Kujawa, M. Lehmann, T. Niermann, State of the art in atomic resolution off-axis electron holography, Ultramicroscopy 116 (2012) 13–23. doi:10.1016/j.ultramic.2012.01.019.
URL `https://doi.org/10.1016/j.ultramic.2012.01.019`

[5] S. Frabboni, G. Matteucci, G. Pozzi, M. Vanzi, Electron holographic observations of the electrostatic field associated with thin reverse-biased $p-n$ junctions, Physical Review Letters 55 (1985) 2196–2199. doi:10.1103/PhysRevLett.55.2196.
URL `https://doi.org/10.1103/PhysRevLett.55.2196`

[6] W. D. Rau, P. Schwander, F. H. Baumann, W. Höppner, A. Ourmazd, Two-dimensional mapping of the electrostatic potential in transistors by electron holography, Physical Review Letters 82 (1999) 2614–2617. doi:10.1103/PhysRevLett.82.2614.
URL `https://doi.org/10.1103/PhysRevLett.82.2614`

[7] R. E. Dunin-Borkowski, M. R. McCartney, R. B. Frankel, D. A. Bazylinski, M. Posfai, P. R. Buseck, Magnetic microstructure of magnetotactic bacteria by electron holography, Science 282 (5395) (1998) 1868–1870. doi:10.1126/science.282.5395.1868.
URL `https://doi.org//10.1126/science.282.5395.1868`

[8] H. S. Park, X. Yu, S. Aizawa, T. Tanigaki, T. Akashi, Y. Takahashi, T. Matsuda, N. Kanazawa, Y. Onose, D. Shindo, A. Tonomura, Y. Tokura, Observation of the magnetic flux and three-dimensional structure of skyrmion lattices by electron holography, Nature Nanotechnology 9 (5) (2014) 337–342. doi:10.1038/nnano.2014.52.
URL `https://doi.org/10.1038/nnano.2014.52`

[9] M. Hÿtch, F. Houdellier, F. Hüe, E. Snoeck, Nanoscale holographic interferometry for strain measurements in electronic devices, Nature 453 (7198) (2008) 1086–1089. doi:10.1038/nature07049.
URL `https://doi.org/10.1038/nature07049`

[10] D. Cooper, J. P. Barnes, J. M. Hartmann, A. Béché, J. L. Rouvière, Dark field electron holography for quantitative strain measurements with nanometer-scale spatial resolution, Applied Physics Letters 95 (5) (2009) 053501. doi:10.1063/1.3196549.
URL `https://doi.org/10.1063/1.3196549`

[11] A. Harscher, H. Lichte, Experimental study of amplitude and phase detection limits in electron holography, Ultramicroscopy 64 (1) (1996) 57–66. doi:10.1016/0304-3991(96)00019-8.
URL `https://doi.org/10.1016/0304-3991(96)00019-8`

[12] D. Cooper, R. Truche, P. Rivallin, J.-M. Hartmann, F. Laugier, F. Bertin, A. Chabli, J.-L. Rouviere, Medium resolution off-axis electron holography with millivolt sensitivity, Applied Physics Letters 91 (14) (2007) 143501. doi:10.1063/1.2794006.
URL `https://doi.org/10.1063/1.2794006`

[13] M. A. Schofield, M. Beleggia, Y. Zhu, G. Pozzi, Characterization of JEOL 2100F Lorentz-TEM for low-magnification electron holography and magnetic imaging, Ultramicroscopy 108 (7) (2008) 625–634. doi:10.1016/j.ultramic.2007.10.015.
URL `https://doi.org/10.1016/j.ultramic.2007.10.015`

[14] E. Voelkl, D. Tang, Approaching routine phase $2\pi/1000$ resolution for off-axis type holography, Ultramicroscopy 110 (5) (2010) 447–459. doi:10.1016/j.ultramic.2009.11.017.
URL `https://doi.org/10.1016/j.ultramic.2009.11.017`

[15] R. A. McLeod, M. Bergen, M. Malac, Phase measurement error in summation of electron holography series, Ultramicroscopy 141 (2014) 38–50. doi:10.1016/j.ultramic.2014.03.001.
URL `https://doi.org/10.1016/j.ultramic.2014.03.001`

[16] T. Niermann, M. Lehmann, Averaging scheme for atomic resolution off-axis electron holograms, Micron 63 (2014) 28–34. doi:10.1016/j.micron.2014.01.008.
URL `https://doi.org/10.1016/j.micron.2014.01.008`

[17] V. Boureau, R. McLeod, B. Mayall, D. Cooper, Off-axis electron holography combining summation of hologram series with double-exposure phase-shifting: Theory and application, Ultramicroscopy 193 (2018) 52–63. doi:10.1016/j.ultramic.2018.06.004.
URL `https://doi.org/10.1016/j.ultramic.2018.06.004`

[18] C. Gatel, J. Dupuy, F. Houdellier, M. J. Hÿtch, Unlimited acquisition time in electron holography by automated feedback control of transmission electron microscope, Applied Physics Letters 113 (13) (2018)

133102. doi:10.1063/1.5050906.
URL `https://doi.org/10.1063/1.5050906`

[19] C. Boothroyd, A. Kovács, K. Tillmann, FEI Titan G2 60-300 HOLO, Journal of large-scale research facilities 2 (A44) (2016). doi:10.17815/jlsrf-2-70.
URL `https://doi.org/10.17815/jlsrf-2-70`

[20] E. Völkl, L. F. Allard, B. Frost, A software package for the processing and reconstruction of electron holograms, Journal of Microscopy 180 (1) (1995) 39–50. doi:10.1111/j.1365-2818.1995.tb03655.x.
URL `https://doi.org/10.1111/j.1365-2818.1995.tb03655.x`

[21] F. Hüe, C. L. Johnson, S. Lartigue-Korinek, G. Wang, P. R. Buseck, M. J. Hÿtch, Calibration of projector lens distortions, Microscopy 54 (3) (2005) 181–190. doi:10.1093/jmicro/dfi042.
URL `https://doi.org/10.1093/jmicro/dfi042`

[22] M. Hÿtch, J. Dupuy, V. Migunov, T. Denneulin, R. Dunin-Borkowski, C. Gatel, Revisiting phase detection limits in electron holography through dynamic automation, in: Proceedings of the European Microscopy Congress 2020, emc2020, Royal Microscopical Society, 2021. doi:10.22443/rms.emc2020.439.
URL `https://doi.org/10.22443/rms.emc2020.439`

[23] Q. Ru, J. Endo, T. Tanji, A. Tonomura, Phase-shifting electron holography by beam tilting, Applied Physics Letters 59 (19) (1991) 2372–2374. doi:10.1063/1.106019.
URL `https://doi.org/10.1063/1.106019`

[24] V. Volkov, M. Han, Y. Zhu, Double-resolution electron holography with simple Fourier transform of fringe-shifted holograms, Ultramicroscopy 134 (2013) 175–184. doi:10.1016/j.ultramic.2013.06.018.
URL `https://doi.org/10.1016/j.ultramic.2013.06.018`

[25] J. M. Hartmann, M. Py, J. P. Barnes, B. Prévitali, P. Batude, T. Billon, Low temperature boron and phosphorous doped SiGe for recessed and raised sources and drains, Journal of Crystal Growth 327 (1) (2011) 68–77. doi:10.1016/j.jcrysgro.2011.05.009.
URL `https://doi.org/10.1016/j.jcrysgro.2011.05.009`

[26] R. M. Langford, A. K. Petford-Long, Preparation of transmission electron microscopy cross-section specimens using focused ion beam milling, Journal of Vacuum Science & Technology A: Vacuum, Surfaces, and Films 19 (5) (2001) 2186–2193. doi:10.1116/1.1378072.
URL `https://doi.org/10.1116/1.1378072`

[27] M. Feuerbacher, Growth of high-entropy alloys, in: Crystal Growth of Intermetallics, De Gruyter, 2018, pp. 141–172. doi:10.1515/9783110496789-007.
URL `https://doi.org/10.1515/9783110496789-007`

[28] Y. Tokunaga, X. Z. Yu, J. S. White, H. M. Rønnow, D. Morikawa, Y. Taguchi, Y. Tokura, A new class of chiral materials hosting magnetic skyrmions beyond room temperature, Nature Communications 6 (1) (jul 2015). doi:10.1038/ncomms8638.
URL `https://doi.org/10.1038/ncomms8638`

[29] D. Cooper, P. Rivallin, G. Guegan, C. Plantier, E. Robin, F. Guyot, I. Constant, Field mapping of focused ion beam prepared semiconductor devices by off-axis and dark field electron holography, Semiconductor

Science and Technology 28 (12) (2013) 125013. doi:10.1088/0268-1242/28/12/125013.
URL `https://doi.org/10.1088/0268-1242/28/12/125013`

Acquisition of object and temperature series in medium resolution off-axis electron holography with live drift correction

Supplementary Information

Thibaud Denneulin[a], Benjamin Zingsem[a], Joseph Vas[a], Wen Shi[a], Luyan Yang[a], Michael Feuerbacher[a] and Rafal E. Dunin-Borkowski[a]

[a]*Ernst Ruska-Centre for Microscopy and Spectroscopy with Electrons, Forschungszentrum Jülich, 52425 Jülich, Germany.*

Supplementary Information 1: Basics of off-axis electron holography

In off-axis electron holography, a voltage is applied to an electron biprism, which is inserted below the sample, generally in the selected area aperture position in order to overlap two electron waves. An interference pattern (the hologram) is recorded on a detector. We consider a reference wave $\psi_1 = A_1 \exp(i\phi_1)$ traveling in a uniform region (vacuum for instance) and an object wave $\psi_2 = A_2(\vec{r}) \exp(i\phi_2(\vec{r}))$ passing through a sample, where $A_1, A_2(\vec{r})$ and $\phi_1, \phi_2(\vec{r})$ are their respective amplitudes and phases. The intensity distribution of an off-axis electron hologram can be expressed

$$I_{holo}(\vec{r}) = A_1^2 + A_2^2(\vec{r}) + I_{\mathrm{inel}}(\vec{r}) + 2\mu A_1 A_2(\vec{r}) \cos(\Delta\phi(\vec{r}) + 2\pi\vec{q_c}.\vec{r}) \ , \tag{1}$$

where $I_{\mathrm{inel}}(\vec{r})$ is the inelastic background, μ is the fringe contrast, $\Delta\phi(\vec{r}) = \phi_1 - \phi_2(\vec{r})$ is the phase change of the object wave with respect to the reference wave and $\vec{q_c}$ is the carrier frequency [1]. The Fourier transform of the hologram can be described as

$$\begin{array}{rcll} \mathrm{FT}\{I_{holo}(\vec{r})\} & = & \mathrm{FT}\{A_1^2 + A_2^2(\vec{r}) + I_{\mathrm{inel}}(\vec{r})\} & \textit{centerband} \\ & & +\mu\mathrm{FT}\{A_1 A_2(\vec{r}) \exp(i\Delta\phi(\vec{r}))\} \otimes \delta(\vec{q} + \vec{q_c}) & \textit{sideband}\ 1 \\ & & +\mu\mathrm{FT}\{A_1 A_2(\vec{r}) \exp(i\Delta\phi(\vec{r}))\} \otimes \delta(\vec{q} - \vec{q_c}) & \textit{sideband}\ 2 \quad . \end{array} \tag{2}$$

Different images can then be reconstructed by using apertures and inverse Fourier transforms such as

$$\begin{array}{rcccll} I_{\mathrm{rec}}(\vec{r}) & = & A_1^2 + A_2^2(\vec{r}) + I_{\mathrm{inel}}(\vec{r}) & & & , \\ C_{\mathrm{rec}}(\vec{r}) & = & \mu A_1 A_2(\vec{r}) \exp(i\Delta\phi(\vec{r})) & & & , \\ A_{\mathrm{rec}}(\vec{r}) & = & \mu A_1 A_2(\vec{r}) & = & \sqrt{Re^2 + Im^2} & , \\ \phi_{\mathrm{rec}}(\vec{r}) & = & \Delta\phi(\vec{r}) & = & \arctan(Im/Re) & , \end{array} \tag{3}$$

where $I_{\mathrm{rec}}(\vec{r})$ is the intensity image reconstructed by applying an aperture to the center-band. $C_{\mathrm{rec}}(\vec{r})$ is the reconstructed complex image obtained after applying an aperture to one of the side-bands, shifting it to center of Fourier space and performing an inverse Fourier transform. $A_{\mathrm{rec}}(\vec{r})$ and $\phi_{\mathrm{rec}}(\vec{r})$ are the corresponding amplitude and phase obtained from the complex image. Usually, the radius of the aperture applied to the side-band is $q_{\mathrm{c}}/3$ to avoid including information from the center-band.

If the effects of dynamical diffraction in the specimen can be neglected and if there are no fringing field outside the specimen, the phase change $\Delta\phi$ is related to electromagnetic fields according to the expression (in one dimension) [2]

$$\Delta\phi(x) = C_E \int V_0(x,z)dz - \frac{e}{\hbar} \iint B_\perp(x,z)dxdz \ , \tag{4}$$

where z is the direction of the incident electron beam, x is a direction perpendicular to z, C_E is an interaction constant that depends on the electron energy, V_0 is the mean inner potential (MIP) of the specimen, $B_\perp$ is the component of the magnetic induction field that is perpendicular to both x and z, e is the electron charge and $\hbar$ is the reduced Planck constant. If V_0 and $B_\perp$ are constant in the specimen along z, then the previous expression can be simplified to

$$\Delta\phi(x) = C_E V_0(x)t(x) - \frac{e}{\hbar} \int B_\perp(x)t(x)dx \ , \tag{5}$$

where t is the specimen thickness. In the case of a non-magnetic sample with uniform thickness, the phase change is proportional to the MIP according to the expression

$$\Delta\phi(x) = C_E V_0(x) t \ . \tag{6}$$

In the case of a magnetic sample with uniform thickness and composition, the derivative of the phase is proportional to the magnetic induction according to the expression

$$\frac{d(\Delta\phi(x))}{dx} = -\frac{e}{\hbar} B_{\perp}(x) \ . \tag{7}$$

Supplementary Information 2: Short description of the stage

Little information could be found about the design of the piezo-enhanced CompuStage. Nonetheless, Fig. S1(a) shows a picture of the stage taken after removal of the cover with the permission of Thermo Fischer Scientific (TFS). Users familiar with TFS microscopes can recognize the beta tilt plug, the red LED on the bottom left that indicates if the holder can be retracted/inserted and the holder entry at the center. The mechanical axes x, y and z are located at the top, left and bottom respectively. After discussion with TFS engineers, we understood that the stage is physically identical to other Titan stages but the piezo control option is obtained using additional cabling during the installation. Three cables controlling the x, y and z piezo components are attached on the right side of the stage. They are visible in Fig. S1(b) when the stage is tilted at a large α angle and they are connected to the mechanical shafts of the three axes. In addition, the piezo stage has its own electronic controller shown in Fig. S1(c) that is installed in a rack next to the microscope PC.

It should be mentioned that the use of a piezo stage in off-axis electron holography has been introduced in previous articles [3, 4], where it was used to scan the sample with respect to the fringes and hence improve the spatial resolution of the reconstructed phase images. However, the piezo components were integrated in a single tilt sample holder [5]. Here, the stage is part of the microscope, which allows different sample holders to be used and hence different experiments to be conducted.

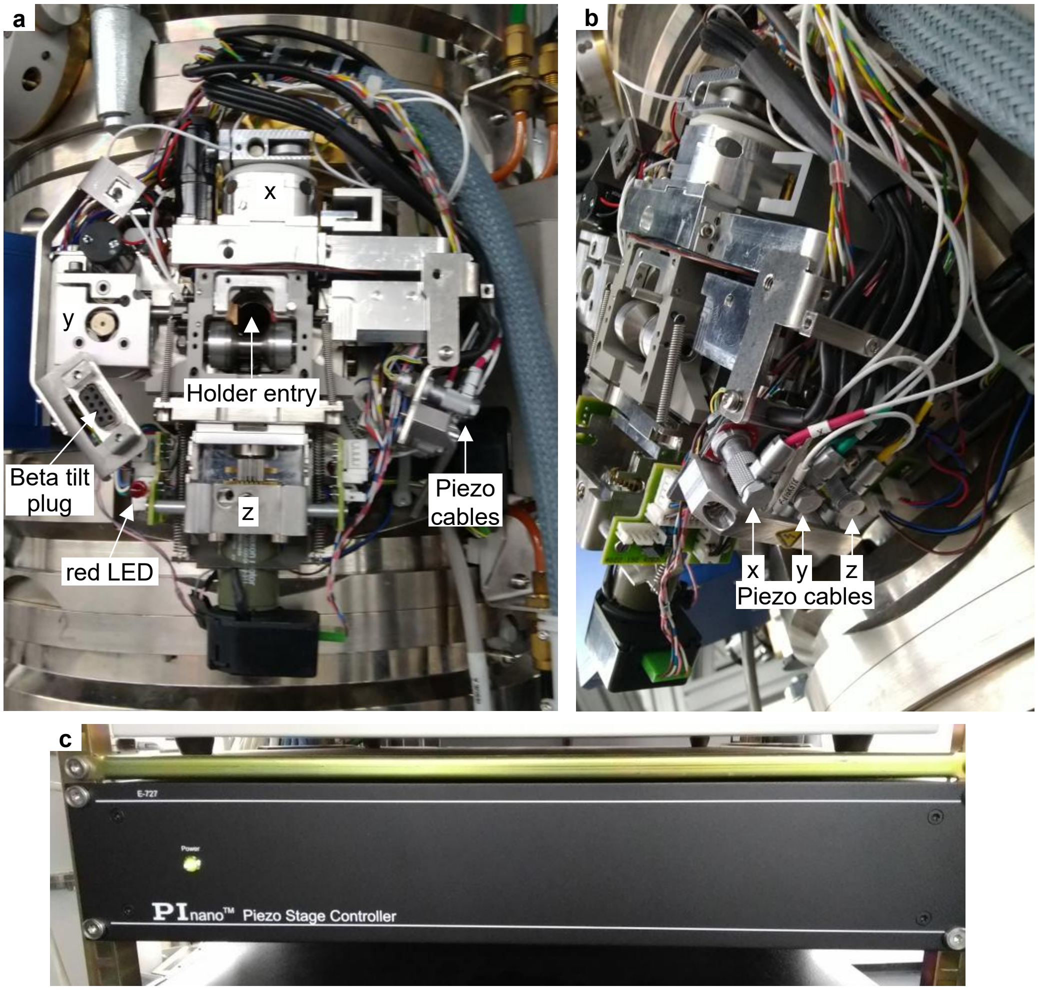

Figure S1: **Pictures of the piezo-enhanced compustage and its controller.** (a) Front-view picture of the compustage oriented at $\alpha = 0°$. (b) Side-view picture with the stage tilted at a large angle to show cables that control the x, y and z piezo components. (c) Electronic controller of the piezo stage.

Supplementary Information 3: Drift correction test using the mechanical and piezo stages

In order to compare the drift correction capabilities of the mechanical and piezo stages, tests have been performed using the two stages separately. Fig. S2(a) shows an image of a cross-grating replica sample with a field-of-view of approximately 600 nm and a pixel size of 0.16 nm. After a calibration step, a continuous correction of the position was set up using the mechanical stage only. Fig. S2(b) shows the distance with respect to the initial sample position and with pixel precision as a function of exposure time. Three displacements of approximately 50, 180 and 130 nm were introduced by moving the stage manually, as indicated by arrows in the plot. It can be observed that the mechanical stage is able to reduce the displacement below 10 nm (see magnified plot at the bottom). However, in the 10 nm range, the position of the sample does not change significantly. Displacements of up to 6 nm, as indicated by a dotted line, remain uncorrected, which suggests that the stage does not respond when such small movements are requested. Fig. S2(c) shows a similar plot obtained using the piezo stage. Again, three perturbations of approximately 50, 40 and 60 nm were introduced by moving the mechanical stage manually. Here, it can be observed that the piezo stage reacts in the sub-10 nm range and is able to reduce small displacements to zero after a few correction steps. The step-wise behavior is related to the fact that the correction factor was set to approximately 80% of the calibrated value. We found that this helps to converge more smoothly because the response of the stage is not always linear.

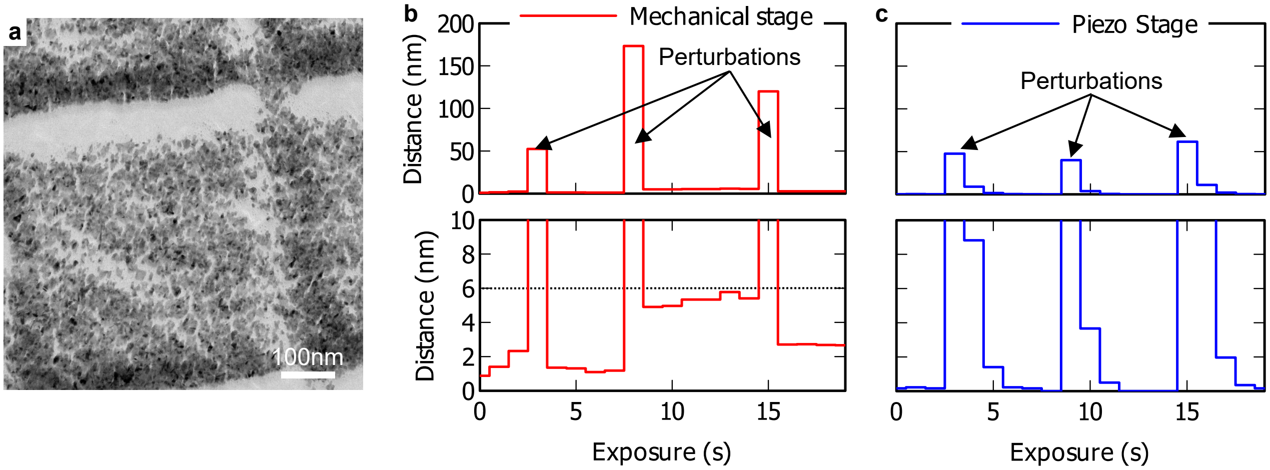

Figure S2: **Drift correction using the mechanical stage.** (a) TEM image of a cross-grating replica sample. (b) Plots that represent the displacement of the sample with respect to its initial position. Three perturbations were introduced as indicated by arrows. The correction is achieved using the mechanical stage. The bottom plot shows a magnified view of the bottom part of the profile. (c) Similar plot but using the piezo stage for correction.

Supplementary Information 4: Calibration of the beam tilt

In order to calibrate the phase shift as a function of beam tilt, we have written a script that collects series of holograms while incrementing the beam tilt with a predefined step. Fig. S3(a) is a schematic diagram that illustrates the influence of the beam tilt on the position of the fringes. Fig. S3(b) is an example of electron hologram obtained in the vacuum and Fig. S3(c) is the Fourier transform calculated in a small region of the hologram, indicated by a dashed square, to minimize computation time. The coordinates of the pixel that has the largest modulus in the side-band are then determined and the corresponding complex value (composed of real Re and imaginary Im parts) is retrieved. For each beam tilt increment, the hologram and the Fourier transform are updated and the phase $\phi = \arctan(Im/Re)$ associated to this pixel is plotted as a function of the input value sent to the beam tilt θ coils (arbitrary units), as shown in Fig. S3(d). The slope of the plot $\Delta\phi/\Delta\theta$ is then calculated to obtain the conversion factor between the phase and the beam tilt. The calibration is performed twice in opposite tilt directions (positive and negative) and the average slope is calculated. This can minimize errors in the case there is a drift of the biprism. In addition, since there are two orthogonal pairs of beam tilt coils (x and y), their respective influence on the phase depends on the orientation of the biprism in the xy plane. In this study, we have first tested the influence of the two pairs of coils for a given orientation of the biprism and used the pair of coils that has the largest influence to minimize the tilt.

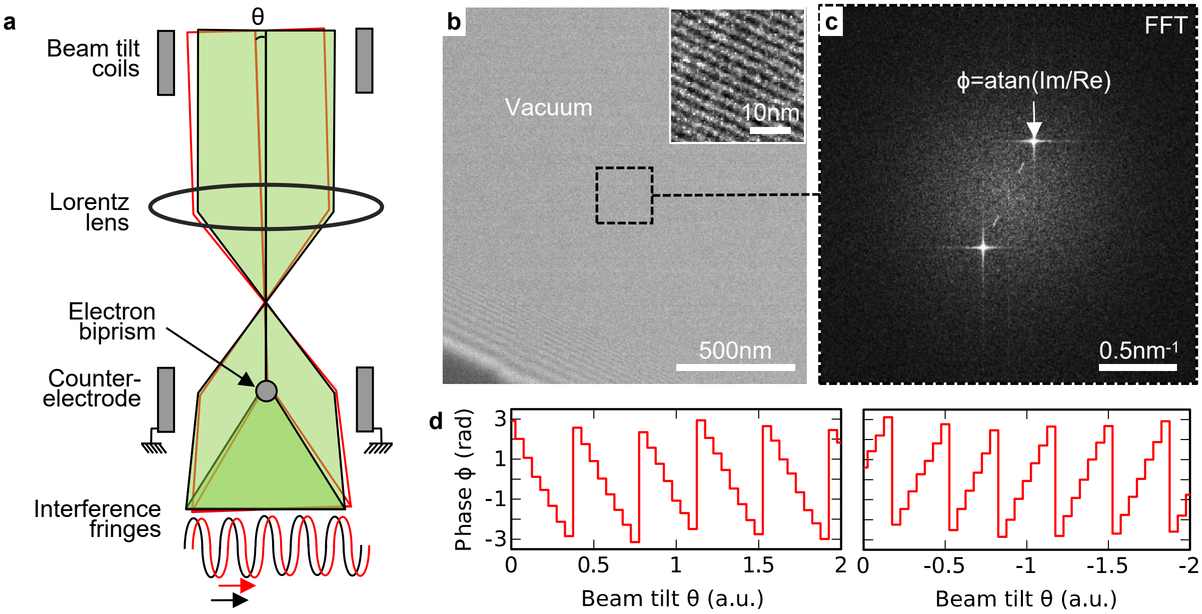

Figure S3: **Calibration of the beam tilt coils.** (a) Schematic diagram that illustrates the relation between the beam tilt θ and the position of the interference fringes in the hologram. (b) Example of electron hologram collected in the vacuum with an exposure time of 0.1 s. The inset in the top-right is a magnified image that shows interference fringes. (c) Fourier transform of the region indicated by a dashed square in (a) and displayed as the modulus of the complex terms. (d) Plots that show the phase (defined in radians and in a 2π range) associated to the pixel of the side-band that has the largest modulus, as a function of the input beam tilt θ (arbitrary unit) for positive and negative tilt directions and with a step of 0.05 a.u..

Supplementary Information 5: Calibration of the piezo stage

In order to calibrate the piezo stage, we have written a script that moves gradually the sample in a given direction and with a predefined increment. The position (x,y) of the sample in the hologram is then determined using cross-correlations of amplitude or phase images which are reconstructed automatically after the acquisition using Fourier transforms [6]. Fig. S4(a) is an example of hologram obtained on a cross-grating replica sample. To save computing time and to avoid possible perturbations from the edges of the holograms, only a small region of the hologram that contains distinct features is selected for the reconstruction. For instance, Fig. S4(b) is the amplitude image corresponding to the region indicated by a dashed square. Fig. S4(c) is a plot that shows the displacement of the sample in x and y directions in the image as a function of the input x_{piezo} value sent to the piezo stage (arbitrary units). For simplicity, it was assumed that the x and y axes are orthogonal and that the response is linear and identical for the two axis. A calibration factor c is determined from the slope of the modulus according to $c = \Delta\left(\sqrt{x^2+y^2}\right)/\Delta x_{\text{piezo}}$. The rotation angle α between the two coordinate systems is determined according to $\alpha = \arctan(y/x)$. Here the rotation angle is relatively small, approximately 0.2 rad, as shown in Fig. S4(d). The relationship between the coordinates of the piezo stage and the coordinates in the image is then obtained via a rotation matrix according to

$$\begin{aligned} x_{\text{piezo}} &= (x\cos(\alpha) + y\sin(\alpha))/c \\ y_{\text{piezo}} &= (-x\sin(\alpha) + y\cos(\alpha))/c\ . \end{aligned} \tag{8}$$

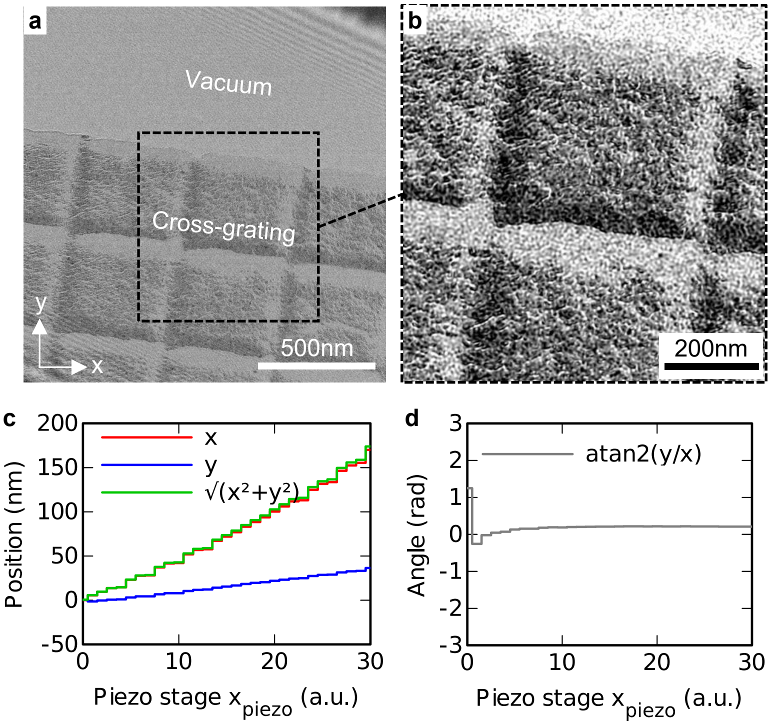

Figure S4: **Calibration of the piezostage.** (a) Example of electron hologram acquired on a cross-grating replica sample. (b) Amplitude image of the region indicated by a dashed square and reconstructed on-the-fly using Fourier transforms. (c) Plot that shows the displacement of the sample in (x,y) coordinates in the image as a function of the input x_{piezo} value of the piezo stage. The modulus $\sqrt{(x^2+y^2)}$ is also plotted. (d) Plot that shows the angle $\alpha = \arctan(y/x)$.

Supplementary Information 6: Acquisition of phase-shifted and double-resolution holograms

Series of phase-shifted holograms can be used to calculate phase images without Fourier transform and hence without aperture limiting the spatial resolution [7, 8]. After the calibration steps described in the previous section, the beam tilt coils were used to acquire phase-shifted holograms with a predefined phase shift and the piezo stage was used to maintain the sample at a fixed position during the acquisition. Fig. S5(a) shows an example of hologram of a cross-grating sample with a fringe spacing of 2.7 nm, a pixel size of 0.41 nm and an exposure time of 20 s. A phase-shifted series of four holograms was acquired with a shift of $\pi/2$ and Fig. S5(b) shows magnified images of the fringes in the vacuum region. For each phase shift, 100 holograms were collected with an individual exposure time of 0.2 s and summed directly during the acquisition. Fig. S5(c) shows three plots that represent the position of the fringes ϕ, the standard deviation of the phase $\delta\phi_{\mathrm{vac}}$ measured in the vacuum region (a corresponding phase image is shown in Fig. S5(d)) and the position of the sample (x,y) as a function of the exposure time. As expected, the phase profile shows four steps shifted by $\pi/2$ with a precision of ±0.1 rad. The profile of the standard deviation $\delta\phi_{\mathrm{vac}}$ shows that the noise decreases continuously with the exposure time and follows the same trend for the four shifts. The (x,y) position profile shows that the position of the sample remains stable with a precision of ±0.41 nm (pixel size), independently of the phase shift.

For a series of N holograms shifted by $2\pi/N$, the phase can be determined by the formula

$$\phi(x, y) = \arctan\left(\frac{\sum I_n \sin(2\pi n/N)}{\sum I_n \cos(2\pi n/N)}\right) - 2\pi q_{\mathrm{c}} x \ , \tag{9}$$

where I_n is the intensity distribution of the holograms, $n = 0, 1, ..., N-1$, q_{c} is the carrier frequency and x is the direction perpendicular to the biprism and to the optical axis [7]. Two phase images were then calculated using Fourier reconstruction of a single hologram and using direct calculation from the phase-shifted series. Fig. S5(e) shows a phase image of the cross-grating region indicated by a green dashed rectangle in (a), obtained using Fourier reconstruction with an aperture size of $q_{\mathrm{c}}/3$. Fig. S5(f) shows a phase image of the same region image obtained using Eq. 9. As expected, finer details can be observed in the last image compared to the previous one, which suggests a finer spatial resolution.

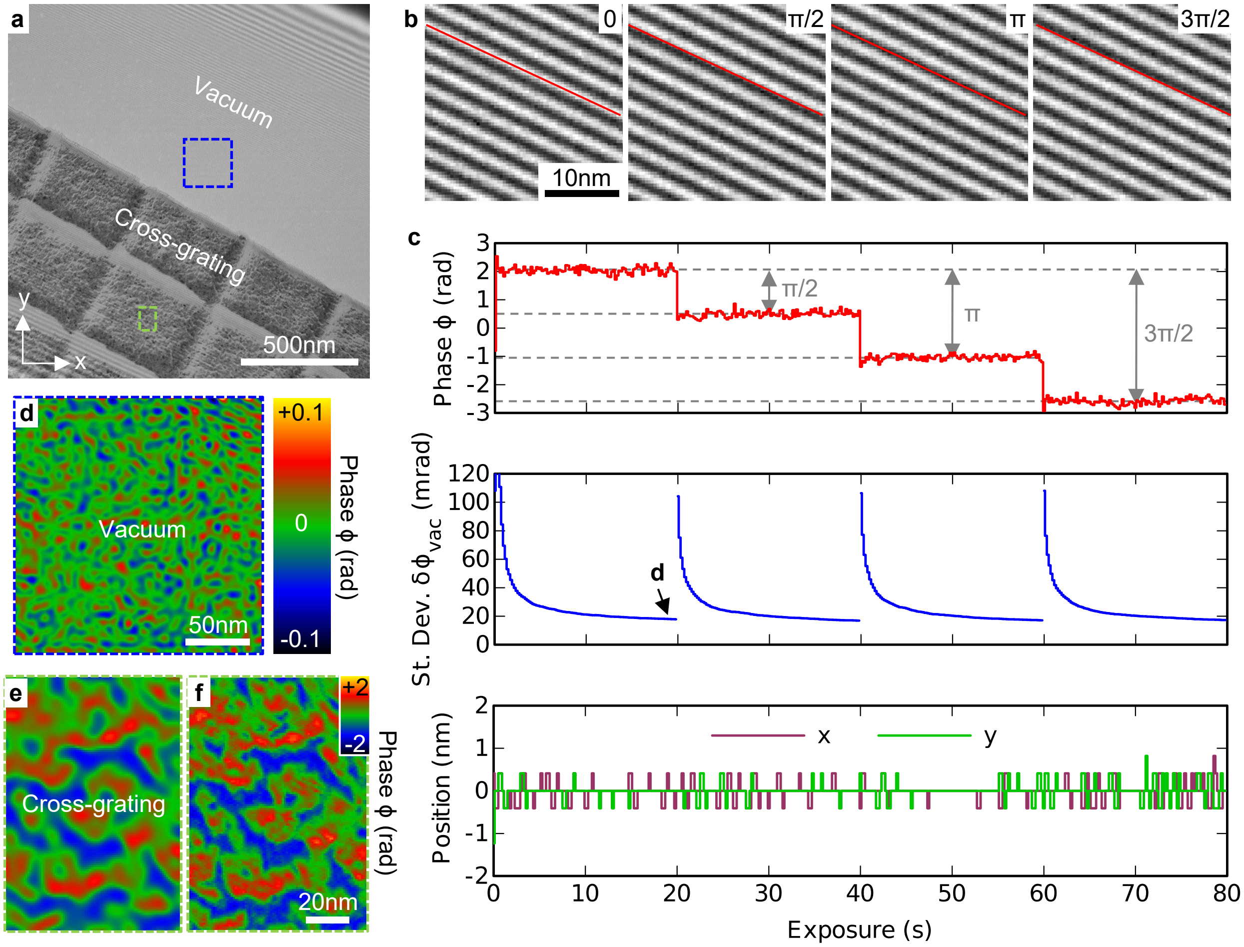

Figure S5: **Acquisition of a drift-corrected phase-shifted series.** (a) Example of electron hologram acquired on a cross-grating replica sample. (b) Magnified images of the interference fringes in four $\pi/2$-phase-shifted holograms. (c) Plots that show the position of the fringes ϕ, the standard deviation of the phase $\delta\phi_{\mathrm{vac}}$ in the vacuum region and the position of the sample (x,y) as a function of exposure time. (d) Example of phase image calculated in the vacuum region indicated by a blue dashed square in (a) where $\delta\phi_{\mathrm{vac}}$ was calculated. (e) Phase images of the cross-grating region indicated by a green dashed rectangle in (a) reconstructed from a single hologram using an aperture size of $q_c/3$. (f) Phase image of the same region reconstructed from the four phase-shifted holograms using direct calculation.

A special case of phase-shifted holography is called double-resolution where two π-shifted holograms are acquired and substracted [9]. This suppresses the center-band and hence allows the use of larger apertures in Fourier space as large as q_c instead of $q_c/3$ or $q_c/2$ for a standard hologram. However, the shift needs to be precisely π, otherwise the contrast of the fringes can be reduced. Fig. S6(a) shows a hologram of a cross-grating with a fringe spacing of 2.7 nm, a pixel size of 0.41 nm and an exposure time of 0.4 s. A magnified view of the fringes is shown on the right side. Fig. S6(b) is a double-resolution hologram obtained with 225 frames of 0.4 s (total exposure 90 s), which shows no background intensity but only variations of intensity caused by the fringes. This is related to the suppression of the center-band in the Fourier transform as shown in Fig. S6(c,d). Fig. S6(e) shows again three plots that represent the position of the fringes ϕ, the standard deviation of the phase $\delta\phi_{\mathrm{vac}}$ measured in the vacuum region and the position of the sample (x,y) as a function of the exposure time. As shown by the phase profile ϕ, the fringes were shifted alternatively by

$+\pi/2$ and $-\pi/2$ between each individual frame of 0.4 s. The double-resolution hologram was then calculated and displayed live during the acquisition. The standard deviation $\delta\phi_{\mathrm{vac}}$ decreases continuously and reaches a similar value as previous ($\approx$ 10 mrad), which indicates there is no loss of contrast associated to the phase shift. Again, the position of the sample (x,y) remained stable over the entire exposure thanks to the drift correction provided by the piezo stage.

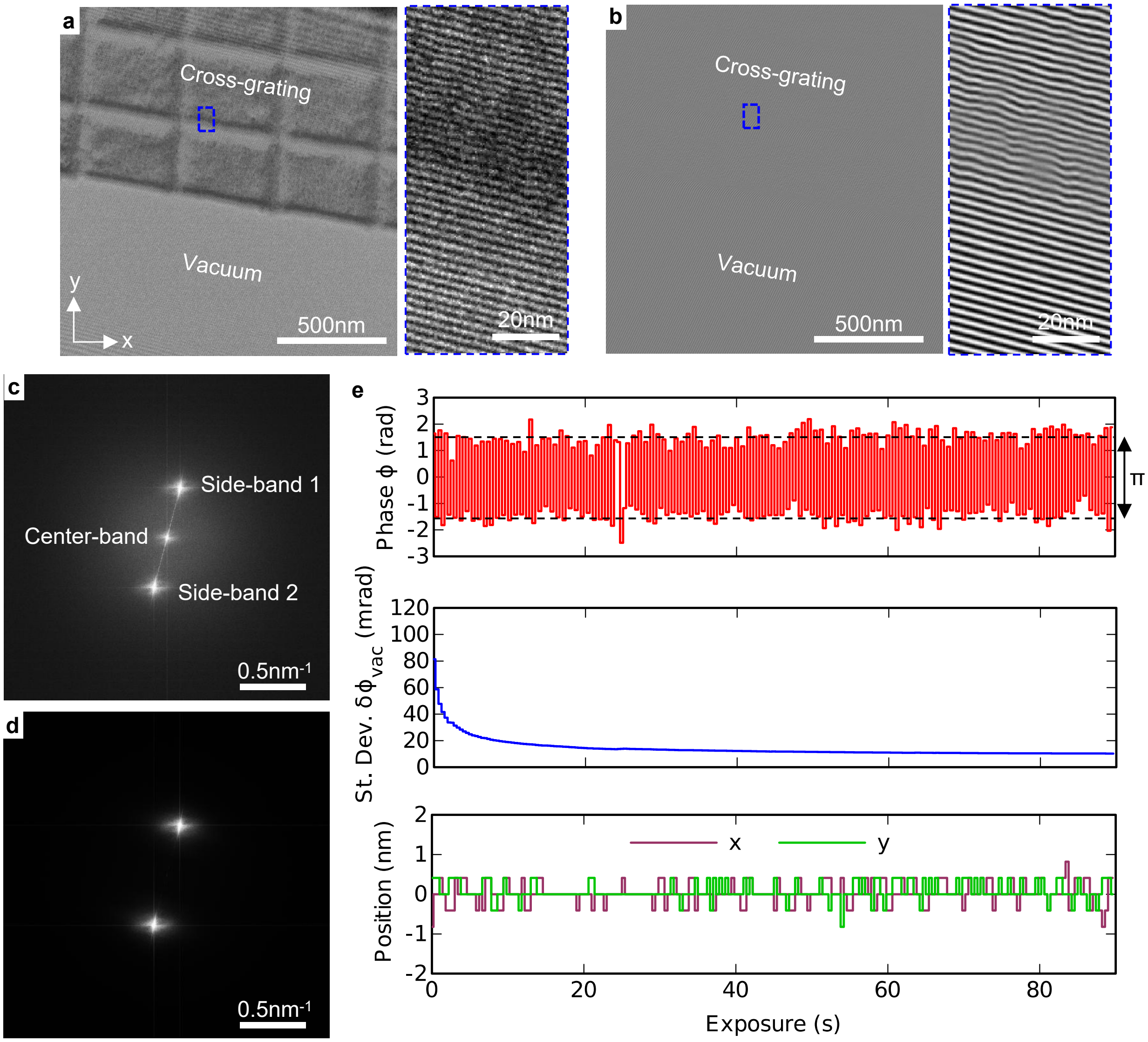

Figure S6: **Acquisition of a double-resolution hologram.** (a) Standard electron hologram acquired on a cross-grating replica sample with an exposure time of 0.4 s. A magnified view of the fringes in the dashed box is shown on the right side. (b) Double-resolution electron hologram of the same area obtained with 225 frames of 0.4 s (total exposure 90 s). (c,d) Fourier transforms of the hologram in (a,b). (e) Plots that show the position of the fringes ϕ, the standard deviation of the phase $\delta\phi_{\mathrm{vac}}$ in the vacuum region and the position of the sample (x,y) as a function of exposure time.

Supplementary Information 7: Acquisition of holograms in objective mode

The experiments shown in the main article and in other sections of the supplement were carried out in Lorentz mode with the excitation of the objective lens of the microscope set to zero. In order to test the drift correction with finer fringes and hence finer spatial resolution, holograms were also acquired using the standard TEM mode where the objective lens is excited. Fig. S7(a) shows an example of hologram obtained on a cross-grating replica sample with a fringe spacing of 0.4 nm, a pixel size of 0.06 nm and a total exposure time of 60 s, without drift correction. 300 frames with an individual exposure time of 0.2 s were collected and summed during the acquisition. The sample is in the bottom-right part of the image and the top-left part shows a vacuum region. Magnified images of the vacuum and sample regions (according to the rectangles in (a)) are shown on the right side. Images with the same settings but with correction of the fringes and sample position are shown in Fig. S7(c). Without correction, the holographic fringes are not visible in the vacuum and only Fresnel fringes can be observed because the holographic fringe contrast is very weak $C = 0.3\%$. With correction, the holographic fringes can be clearly observed with a contrast of $C = 13\%$. In both cases crystal lattice fringes can be seen in the magnified image of the sample but the low mag image without correction appears more blurry than the one with correction due to a drift of the sample. Fig. S7(b,d) shows unwrapped phase images of the entire holograms in (a,c). Because of the very low fringe contrast in (a), the uncorrected phase (b) shows a large number of unwrapping errors and a strong background noise with a standard deviation of $\delta\phi_{\text{vac}} = 928$ mrad in the vacuum region. On the other hand, the corrected phase (d) is much smoother with $\delta\phi_{\text{vac}} = 40$ mrad.

For more details, Fig. S7(e) show different plots that represent the position of the fringes ϕ, the standard deviation of the phase $\delta\phi_{\text{vac}}$ in the vacuum and the position of the sample (x,y) as a function of exposure time. Without correction, the position of the fringes ϕ drifted several times over π, which causes the contrast and hence the standard deviation $\delta\phi_{\text{vac}}$ to oscillate. With correction, the position of the fringes ϕ remains constant with a precision of ±0.3 rad. $\delta\phi_{\text{vac}}$ decreases continuously following an inverse relationship and tends towards a limit of approximately 40 mrad. Regarding the position of the sample (x,y), without correction the drift reached up to 2 nm in x and 12 nm in y during the entire experiment. With correction, the position of the sample was maintained fixed with a precision of ±0.2 nm.

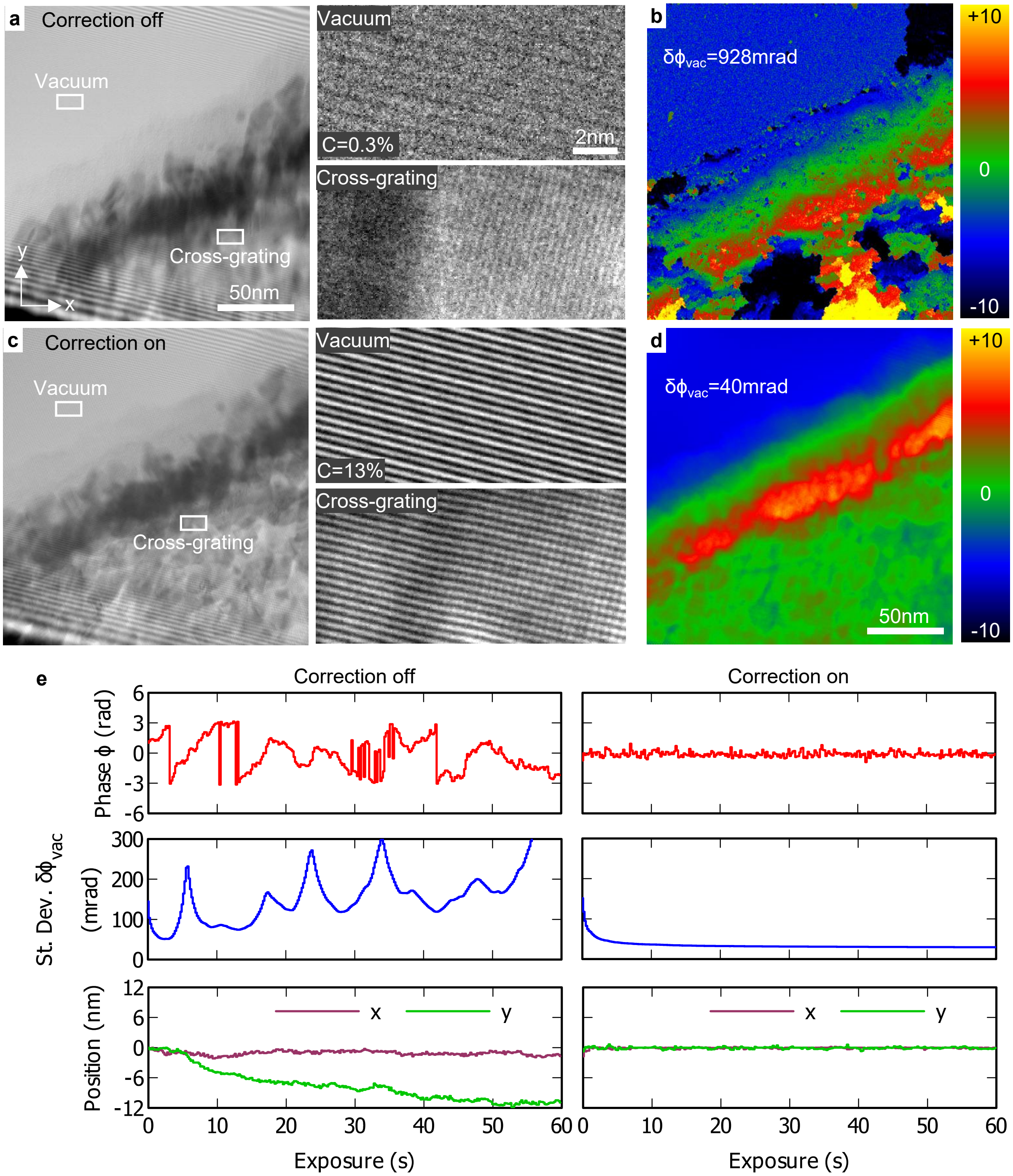

Figure S7: **Acquisition of holograms in objective mode.** (a) Off-axis electron hologram of a cross-grating replica sample recorded in objective mode for 60 s without any correction. Magnified images of the hologram in the vacuum and cross-grating region indicated by rectangles are shown on the right. (b) Corresponding phase image reconstructed using Fourier processing with an aperture size of $q_c/3$. (c) Off-axis electron hologram recorded for 60 s with correction of the fringe position using the beam tilt and correction of the sample position using the piezo stage. Magnified images of the hologram in the vacuum and cross-grating regions indicated by rectangles are shown on the right. (d) Corresponding phase image. (e) Plots that show the position of the fringes ϕ, the standard deviation of the phase $\delta\phi_{\mathrm{vac}}$ in the vacuum region and the position of the sample (x,y) as a function of exposure time, without (left) and with correction (right).

Supplementary Information 8: Cross-correlation of images reconstructed from holograms of a transistor

In order to find correct settings for the cross-correlation of images of transistors shown in the main article (in section 3.3.2) , preliminary tests have been performed with different images. Fig. S8(a) shows a hologram of a transistor and reconstructed images including the intensity $I_{\text{rec}}(\vec{r})$, the amplitude $A_{\text{rec}}(\vec{r})$ and the phase $\phi_{\text{rec}}(\vec{r})$ as described in Eq. 3. In Fig. S8(b), the hologram was shifted numerically by approximately 170 nm, as indicated by a white arrow. The same series of images was reconstructed from the shifted hologram. Cross-correlations were then performed for each type of image as shown in Fig. S8(c). The arrows indicate the position of the maximum. It was found that only the cross-correlation of the phase images (ϕ_{rec}) shown in the last column gives the correct value of the shift. The other images led to distant results.

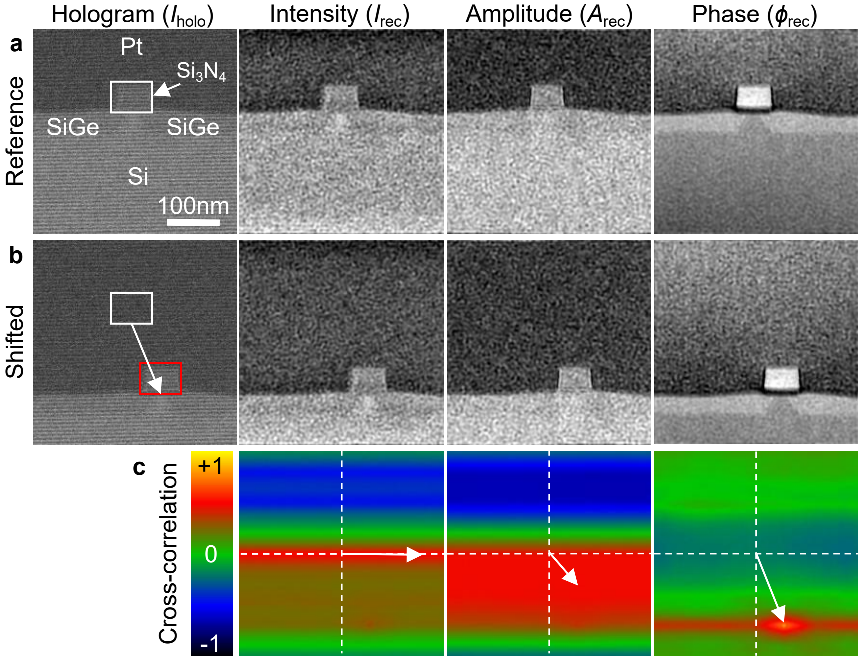

Figure S8: **Cross-correlation of images of transistors.** (a) Off-axis electron hologram of a dummy MOSFET transistor and reconstructed images including the intensity $I_{\text{rec}}(\vec{r})$, the amplitude $A_{\text{rec}}(\vec{r})$ and the phase $\phi_{\text{rec}}(\vec{r})$. (b) Same hologram as in (a) but shifted by 170 nm, as indicated by a white arrow, and corresponding series of reconstructed images. (c) Corresponding series of cross-correlation images where the arrows indicate the position of the maximum.

References

[1] H. Lichte, M. Lehmann, Electron holography - basics and applications, Reports on Progress in Physics 71 (1) (2008) 016102. doi:10.1088/0034-4885/71/1/016102.
URL `https://doi.org/10.1088/0034-4885/71/1/016102`

[2] M. R. McCartney, D. J. Smith, Electron holography: Phase imaging with nanometer resolution, Annual Review of Materials Research 37 (1) (2007) 729–767. doi:10.1146/annurev.matsci.37.052506.084219.
URL `https://doi.org/10.1146/annurev.matsci.37.052506.084219`

[3] D. Lei, K. Mitsuishi, K. Harada, M. Shimojo, D. Ju, M. Takeguchi, Direct acquisition of interferogram by stage scanning in electron interferometry, Microscopy 62 (6) (2013) 563–570. doi:10.1093/jmicro/dft032.
URL `https://doi.org/10.1093/jmicro/dft032`

[4] D. Lei, K. Mitsuishi, K. Harada, M. Shimojo, D. Ju, M. Takeguchi, Super-resolution phase reconstruction technique in electron holography with a stage-scanning system, Japanese Journal of Applied Physics 53 (2S) (2014) 02BC23. doi:10.7567/jjap.53.02bc23.
URL `https://doi.org/10.7567/jjap.53.02bc23`

[5] M. Takeguchi, A. Hashimoto, M. Shimojo, K. Mitsuishi, K. Furuya, Development of a stage-scanning system for high-resolution confocal STEM, Journal of Electron Microscopy 57 (4) (2008) 123–127. doi:10.1093/jmicro/dfn010.
URL `https://doi.org/10.1093/jmicro/dfn010`

[6] E. Völkl, L. F. Allard, B. Frost, A software package for the processing and reconstruction of electron holograms, Journal of Microscopy 180 (1) (1995) 39–50. doi:10.1111/j.1365-2818.1995.tb03655.x.
URL `https://doi.org/10.1111/j.1365-2818.1995.tb03655.x`

[7] Q. Ru, J. Endo, T. Tanji, A. Tonomura, Phase-shifting electron holography by beam tilting, Applied Physics Letters 59 (19) (1991) 2372–2374. doi:10.1063/1.106019.
URL `https://doi.org/10.1063/1.106019`

[8] Q. Ru, G. Lai, K. Aoyama, J. Endo, A. Tonomura, Principle and application of phase-shifting electron holography, Ultramicroscopy 55 (2) (1994) 209–220. doi:10.1016/0304-3991(94)90171-6.
URL `https://doi.org/10.1016/0304-3991(94)90171-6`

[9] V. Volkov, M. Han, Y. Zhu, Double-resolution electron holography with simple Fourier transform of fringe-shifted holograms, Ultramicroscopy 134 (2013) 175–184. doi:10.1016/j.ultramic.2013.06.018.
URL `https://doi.org/10.1016/j.ultramic.2013.06.018`